

Photoplethysmograph Fingernail Sensors for Measuring Finger Forces Without Haptic Obstruction

Stephen A. Mascaro, *Student Member, IEEE*, and H. Harry Asada, *Member, IEEE*

Abstract—A new type of touch sensor for detecting contact pressure at human fingertips is presented. Unlike traditional electronic gloves, in which sensor pads are placed between the fingers and the environment surface, this new sensor allows the fingers to directly contact the environment without obstructing the human's natural haptic senses. The finger touch force is detected by measuring changes in the coloration of the fingernail; hence the sensor is mounted on the fingernail rather than on the fingertip. Specifically, the fingernail is instrumented with miniature light emitting diodes (LEDs) and photodetectors in order to measure changes in the reflection intensity when the fingertip is pressed against a surface. The changes in intensity are then used to determine changes in the blood volume under the fingernail, a technique termed "reflectance photoplethysmography." A hemodynamic model is used to investigate the dynamics of the blood volume at two locations under the fingernail. A miniaturized prototype nail sensor is designed, built, and tested. The theoretical analysis is verified through experiment and simulation.

Index Terms—Touch sensor, haptic, touch force, fingernail, fingertip, plethysmograph, photoplethysmograph, photo sensor, electronic glove, touch input, finger force.

I. INTRODUCTION

THERE IS AN increasing need for measuring forces acting between human hands and the environment. In particular, forces acting at the fingertip are critically important for understanding human manipulation [1], [2], acquiring skills [3], monitoring human behavior [4], and understanding human intentions [5], [6].

External finger forces are measured by placing force-sensing pads at the fingertips. A wide variety of such pads have been developed in the past for applications in robotics and medicine [7], using resistive, capacitive, piezoelectric, or optical elements to detect force. These pads have often been placed in electronic gloves in order to monitor human behavior during manipulation. Yun *et al.* placed force-sensing resistors within a CyberGlove for teleoperation [5]. Sato *et al.* placed conductive rubber pressure sensors within a CyberGlove or DataGlove in order to analyze human grasping [2]. Mascaro *et al.* placed force-sensing resistors in an electronic glove in order to monitor the human state during a cooperative assembly task with a robot [6]. Electronic

Manuscript received January 7, 2000; revised August 21, 2000 and July 29, 2001. This paper was recommended for publication by Associate Editor A. Bicchi and Editor S. Salcudean upon evaluation of the reviewers' comments.

The authors are with the d'Arbelloff Laboratory for Information Systems and Technology, Department of Mechanical Engineering, Massachusetts Institute of Technology, Cambridge, MA 02139 USA (e-mail: smascaro@mit.edu; asada@mit.edu.).

Publisher Item Identifier S 1042-296X(01)10087-X.

gloves in general have been used increasingly in the robotics and virtual reality communities for a variety of human-machine interactions [8].

A critical problem with these force sensors is that they are often bulky and inevitably deteriorate the human haptic sense, since the fingers cannot directly touch the environment surface. Recently, much research has focused on reducing this problem by inventing thinner and more flexible force-sensing pads [9]–[11].

In this paper, a new approach to the detection of finger forces is presented in order to completely eliminate any impediment to the natural haptic sense. Namely, the finger force is measured without having to place any sensor pad between the finger skin and the environment surface. Instead, the force is detected by an optical sensor mounted on the fingernail. This allows the human to touch the environment with bare fingers and perform fine, delicate tasks using the full range of haptic sense. Miniaturized optical components and circuitry allow the sensor to be disguised as a decorative fingernail covering.

First, this paper will describe the basic principles and construction of the reflectance photoplethysmograph fingernail sensors. Next, an anatomically based, lumped-parameter, hemodynamic model is constructed to explain the change in reflection intensity at two locations on the fingernail. Dynamic equations are derived for the model, and static and dynamic simulation results are presented. A prototype nail sensor is then designed and built, and experiments are performed to measure the actual static and dynamic responses of the sensor for several subjects. Experimental and simulated responses are compared in order to evaluate the model. Results of the comparison and their impact on sensor performance are discussed.

II. PRINCIPLE

A. Color Changes in Fingernails

Fig. 1 shows the cross section of an ordinary human fingertip and its fingernail. As the fingertip is pressed down on a surface with increasing force, the blood flow through the fingertip is affected, and a sequence of color changes is observed through the fingernail. In fact, the color change is characteristically nonuniform along the length of the nail, resulting in distinct patterns of color change. These color patterns can be measured by placing arrays of micro LEDs and photodetectors on the nail.

Fig. 2 shows a typical sequence of observable color changes with increasing touch force. Although the force thresholds may vary from person to person, the underlying physiological prin-

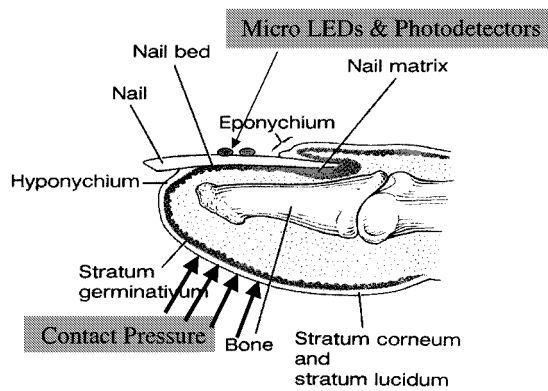


Fig. 1. Pressure applied to the fingertip (adapted from [12] by permission).

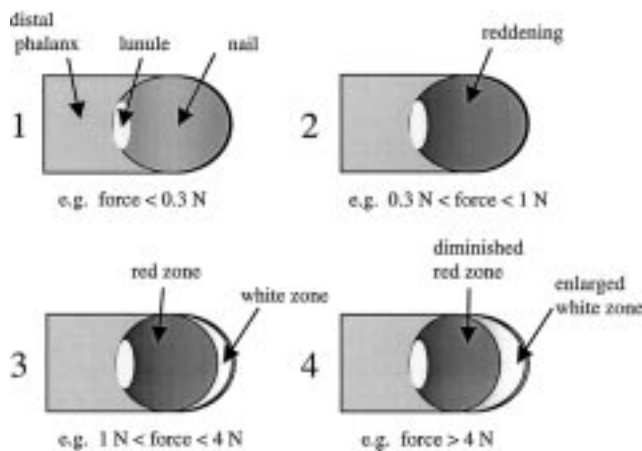


Fig. 2. Typical fingernail color changes.

principle is universally applicable for a healthy fingernail in an ordinary environment.

Above a certain threshold, e.g., 0.3 N, the entire nail begins to redden in color. The cause of this phenomenon lies in the blood flow through the fingertip, the details of which will be explained in Section III. Forces within the 0.3–1 N range are sufficient to cause the venous return of blood in the fingertip to be progressively constricted. This results in pooling of arterial blood in the capillaries underneath the fingernail. This arterial blood is rich in oxyhemoglobin and is therefore bright red in color. When the touch force reaches a certain point, e.g., 1 N, the veins are completely blocked and the fingernail color stops reddening with further increase in touch pressure.

Further increases in the touch force begin to push all blood out of the very tip of the finger, resulting in a white band at the front of the nail. As the force increases, the white band widens until some limit is reached, e.g., at 4 N. Increases in touch force beyond this point have no visible effect. However, forces applied longitudinally to the front of the fingertip and shear forces applied along the length of the finger are more effective at exerting stresses on the tissue above the bone, and are capable of increasing the white band even further.

B. Construction of the Nail Sensors

The phenomenon described above can be utilized to measure touch force or contact pressure by monitoring changes in fingernail coloration without having to put a sensor between the finger

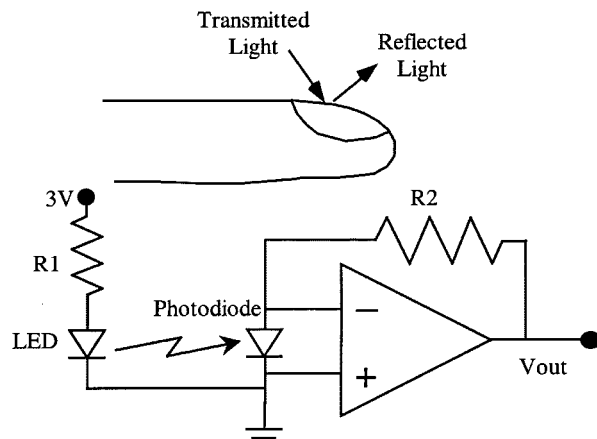


Fig. 3. Photoplethysmograph fingernail sensor.

and the surface. The change in color is directly related to the change in volume of blood underneath the fingernail. The amount of blood under the fingernail bed can be monitored by shining light into the fingernail and measuring the intensity of reflected light, a technique termed “reflectance photoplethysmography.”

Fig. 3 shows the basic construction of the photoplethysmograph fingernail sensor. An LED illuminates the nail bed with light. A photodiode is mounted nearby and detects the reflected light from the nail bed. As contact pressure increases, more arterial blood accumulates under the nail. The additional volume of blood under the nail tends to increase the absorption of light. As more light is absorbed, less light is reflected, and the magnitude of the output voltage of the photodiode circuit, $|V_{out}|$, decreases.

The absorption of light is also dependent on the oxygen concentration in the blood and the wavelength of the light. Fig. 4 shows the absorption characteristics of blood, which consists mainly of oxyhemoglobin (HbO_2) and reduced hemoglobin (Hb). The extinction coefficients of these two components differ on either side of the isobestic wavelength (800 nm). By using two LEDs of different wavelengths, e.g., 660 and 940 nm, the concentration of oxygen in the blood can be determined from the ac components of the two plethysmographs [13], a technique termed “pulse oximetry.” The two LEDs are illuminated alternately and the reflected light is measured by the same photodiode with the aid of sample-and-hold circuitry. If only the volume of blood is of interest, a single LED at the isobestic wavelength will provide measurements that are decoupled from the effect of oxygen concentration. Hence, this isobestic wavelength is chosen for measuring finger forces, although other wavelengths may also be satisfactory.

III. VASCULAR ANATOMY AND HEMODYNAMIC MODELING

A. Fingertip Anatomy

Fig. 2 showed the typical change in coloration of the fingernail with increasing touch force at the fingertip. In order to understand the correlation between the touch force and the observed behavior, a hemodynamic model of the blood flow in the fingertip will be created and verified. The goal is a model that can predict the magnitude and location of an input force, based on the measurable change in reflection intensity. As a first step toward a model that meets all of the above specifica-

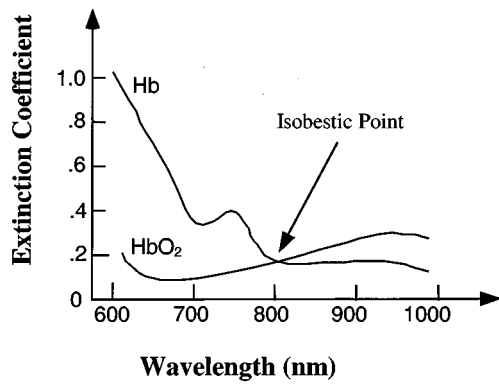


Fig. 4. Blood absorption characteristics.

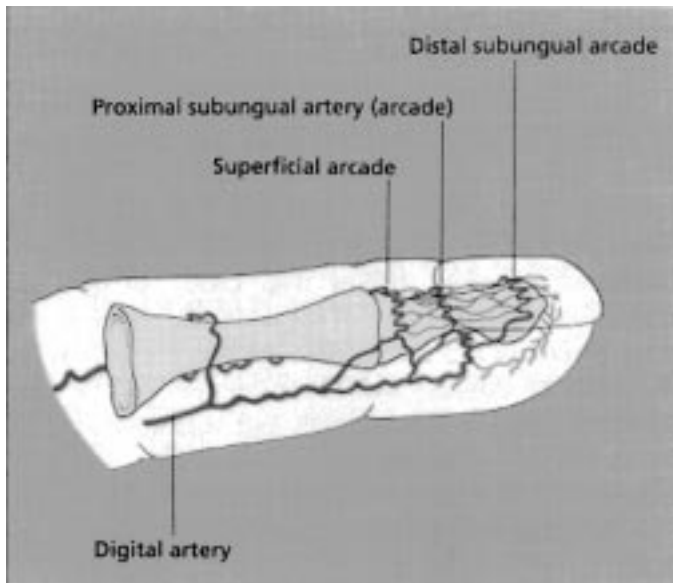


Fig. 5. Arterial anatomy of the fingertip (adapted from [14] by permission).

tions, a lumped-parameter model will be created that explains the changes in blood volume and reflection intensity at both the reddening zone and the whitening zone from a limited set of force locations. In order to construct a realistic, physically based, lumped-parameter model, the first step is to examine the anatomy of the blood vessels in the fingertip.

A variety of details on the vascular anatomy of the fingertip can be found in several sources such as [15]–[19]. The nail bed is richly vascularized with blood flowing from the digital arteries into a network of arterioles, through capillary loops just under the surface, and back out through the venules to the digital veins. Figs. 5 and 6 show the anatomy of the digital arteries and veins. As seen in Fig. 5, the main digital arteries divide into a network of smaller arteries that run principally above the bone, which is connected to the fingernail via a strong matrix of collagen and elastic fibers. The nails are thus described as “immobile over the distal phalange” [15]. As a result, the arteries underneath the nail are protected from touch pressure, allowing uninterrupted supply of blood to the capillaries under the nail. However, the flow of blood out of the fingertip relies largely on the lateral ramifications of the digital veins shown in Fig. 6, [20]. In addition, the veins are generally larger and more compliant than the arteries, leaving them susceptible to collapse by

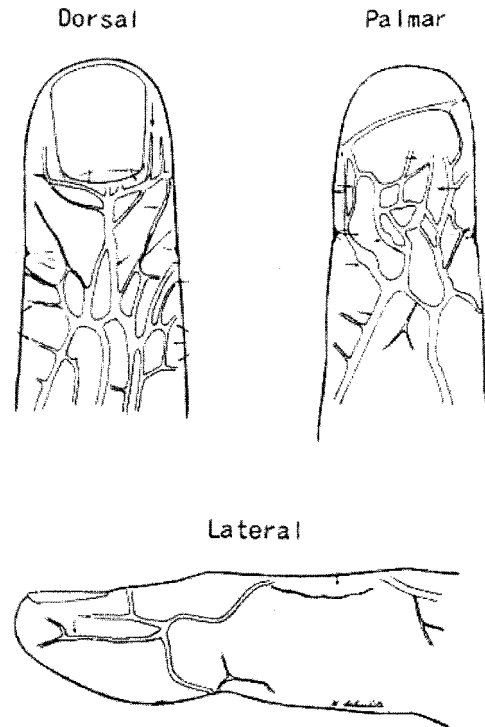


Fig. 6. Venous anatomy of the fingertip (adapted from [20] by permission).

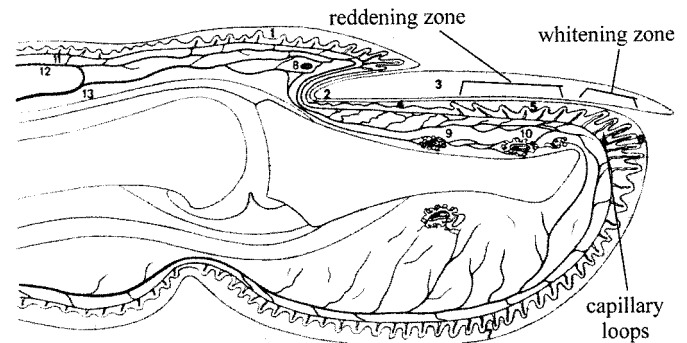


Fig. 7. Capillaries of the fingertip (adapted from [16] by permission).

touch pressure [21]. As a result, when touch pressure is applied to the fingertip, the veins are collapsed, causing blood to pool up in the capillaries underneath the nail.

The capillaries run longitudinally under the nail bed and are twice as long and twice as numerous as those in the pulp on the palmar side of the fingertip, as shown in Fig. 7, [16]. Thus the blood that pools up in the capillaries of the nail bed is highly visible and is responsible for the reddening effect described earlier. Fig. 7 also shows that the capillaries under the nail at the tip of the finger are not protected by the bone. Thus touch pressure can propagate around the tip of the bone, causing these capillaries to collapse and pushing all of the blood out of them. This results in the whitening effect described earlier.

B. Hemodynamic Network Model

Based on the anatomical behavior described above, a lumped-parameter, hemodynamic model that captures both reddening and whitening phenomena will be formed in this section. Three major components are needed for elucidating the hemodynamic behavior: 1) capillaries where the visible blood volume changes

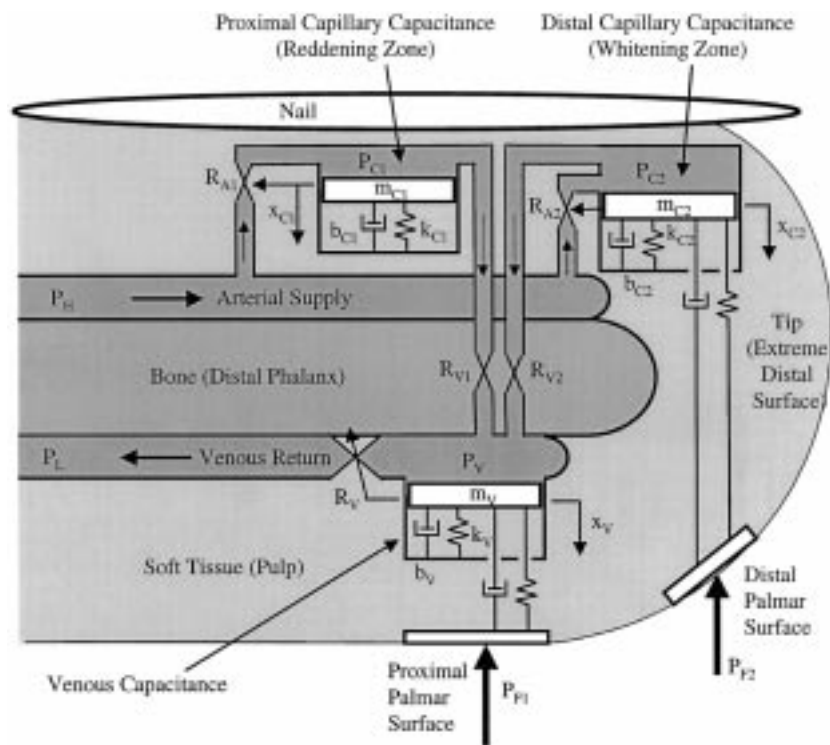


Fig. 8. Hemodynamic model of the fingertip.

occur; 2) arterial supply and venous return; and 3) a mechanism that varies fluidic resistance and capacitance in response to pressures applied at the fingertip.

1) *Capillaries:* There are two distinct zones of capillaries: the proximal reddening zone capillaries that are protected by the nail-bone structure, and the distal whitening zone capillaries that are susceptible to collapse by applied pressure. The capillary network must be lumped to create two separate capacitive elements in the model, corresponding to these two zones. Fig. 8 shows the schematic of the lumped-parameter model containing two capacitances representing the lumped capillaries of the reddening and whitening zones.

2) *Arterial Supply and Venous Return:* It is known that the fluidic resistance of the capillaries is an order of magnitude higher than that of the digital arteries and veins [21]. Therefore, the pressure drop along the arterial supply and venous return is negligible, and hence all the arteries and veins can be lumped into single flows from which the capillaries branch out in parallel, as shown in Fig. 8. Unlike the arteries, the veins are not protected by the bone, so the venous return is modeled with a capacitive element while the arterial supply is not.

3) *Variation of Fluidic Resistance and Capacitance:* The fluidic resistances and capacitances of the capillaries and veins vary in response to the pressures applied to the finger. As shown in Fig. 8, the venous wall is modeled as a mass-spring-damper system with parameters $m_V, k_V,$ and $b_V,$ respectively. Likewise, the capillary walls are modeled as mass-spring-damper systems with parameters $m_{C1}, m_{C2}, k_{C1}, k_{C2}, b_{C1}$ and $b_{C2}.$ The walls deviate from their effective nominal diameters $D_V, D_{C1},$ and D_{C2} by the displacements $x_V, x_{C1},$ and $x_{C2}.$ When pressure P_{F1} acts on the proximal palmar surface of the fingertip, the wall is displacement, x_V becomes increasingly

negative. As the effective venous diameter, $D_V + x_V,$ is thus reduced, the fluidic resistance of the venous return, $R_V,$ increases. This causes the pressures in the capillary elements, P_{C1} and $P_{C2},$ to increase, which then increases the displacements of the capillary walls, $x_{C1},$ and $x_{C2}.$ As the effective diameters $D_{C1} + x_{C1}$ and $D_{C2} + x_{C2}$ thus increase, more blood is stored in the capillaries, resulting in the reddening effect. Changes in $x_{C1},$ and x_{C2} also modulate the fluidic resistances in the capillary elements, R_{A1} and $R_{A2},$ which further magnifies the reddening effect.

Behavior of the distal capillary capacitance at the whitening zone, however, differs from the proximal one when pressure P_{F2} acts on the distal palmar surface of the fingertip. Since the bone does not extend all the way to the tip of the finger, pressure P_{F2} directly propagates through the tissue at the fingertip, resulting in a decrease in the displacement of the distal capillary wall, $x_{C2}.$ In consequence, the effective diameter $D_{C2} + x_{C2}$ is reduced and blood is removed from the distal capillary capacitance, causing the whitening effect.

At this stage a few assumptions underpinning the above hemodynamic model will be made.

- 1) The soft tissue (pulp) of the finger can be treated as a virtually fluidic medium to the extent that external pressure on the fingertip is propagated directly to the veins and to the capillaries at the front of the nail. Such “waterbed” models have been used in the past to model the fingertip [22].
- 2) The bone and nail bed matrix effectively shield the arterial supply and capillaries under the rear portion of the nail from the direct influence of touch forces (see Figs. 5 and 7).
- 3) The effects of shear forces and finger bending are neglected.

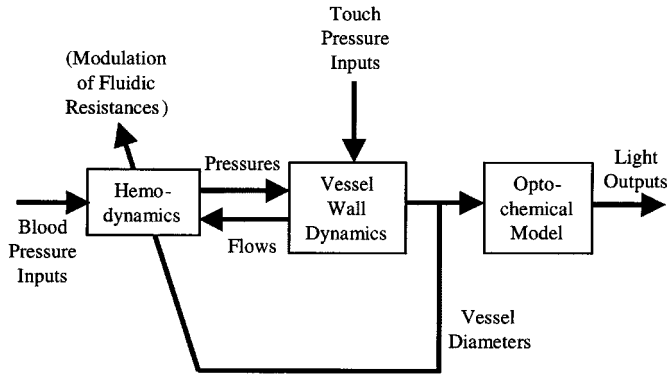


Fig. 9. Model interactions.

The model can eventually be expanded to include more than two capillary units, depending on the hemodynamic behavior of interest and the number of photodetectors that are to be placed on the nail. The number of locations where input forces are applied can also be expanded, given a more thorough treatment of the tissue mechanics.

Fig. 9 shows a block diagram representation of the fingernail and sensor system that highlights the inputs and outputs, and the interactions between the hemodynamics and vessel wall dynamics. They not only interact through the fluidic pressures and flows at the capillary and venous walls, but also through the modulation of the fluidic resistances by the capillary and venous diameters, as shown by the feedback loop in the figure. It is this nonlinear effect of the modulation that is responsible for the redening phenomenon. The primary inputs to the system are touch pressures, P_{F1} and P_{F2} , while the outputs are the light intensities detected by the photodetectors. Blood pressures P_H and P_L act on the system as secondary inputs or disturbances.

IV. STATE EQUATIONS AND DYNAMIC SIMULATION

A. State Equations and Output Function

In this section, dynamic state equations and output function will be derived for the hemodynamic network model obtained above. Simple constitutive laws will be assumed for the elements involved in the lumped-parameter model. The system contains six elements that store energy independently; these are the blood vessel capacitances, k_{C1} , k_{C2} , and k_V , and the masses of the blood vessel walls and blood, m_{C1} , m_{C2} , and m_V . The state variables that are used for locating the dynamic state of the system are the effective displacements of the capillary and venous walls, x_{C1} , x_{C2} , and x_V , and their time rates of change. Therefore a total of six state variables are needed:

$$\mathbf{x} = [x_{C1} \ x_{C2} \ x_V \ \dot{x}_{C1} \ \dot{x}_{C2} \ \dot{x}_V]^T. \quad (1)$$

As shown in Fig. 9, the inputs to the system consist of the upstream and downstream blood and the external touch pressures applied to the fingertip:

$$\mathbf{u} = [P_H \ P_L \ P_{F1} \ P_{F2}]^T. \quad (2)$$

The flow in the fingertip is of low Reynold's number. Therefore the fluidic resistances can be modeled using laminar pipe flow [21]. The lumped capillary and venous resistances are

given by

$$\begin{aligned} R_{A1}(\mathbf{x}) &= \frac{128L_{C1}\mu_{\text{Blood}}}{N_{C1}\pi(D_{C1} + x_{C1})^4} \\ R_{A2}(\mathbf{x}) &= \frac{128L_{C2}\mu_{\text{Blood}}}{N_{C2}\pi(D_{C2} + x_{C2})^4} \\ R_V(\mathbf{x}) &= \frac{128L_V\mu_{\text{Blood}}}{N_V\pi(D_V + x_V)^4}. \end{aligned} \quad (3)$$

Note that the resistances are functions of the state variables, and are hence modulated by the blood vessel diameters. These are prominent nonlinearities characteristic to the fingernail sensor system. The stiffness and damping characteristics of blood vessels are generally nonlinear. To analyze pulsation of hemodynamic behavior, this nonlinearity must be taken into account. The nail sensor dynamics, however, are not heavily dependent on the pulsatile dynamics, since the dc components of the photodetector outputs are used rather than the ac components. Therefore, linear compliance and damping are used for the blood vessels in this paper. The state equations are therefore given by

$$\dot{\mathbf{x}} = \mathbf{A}(\mathbf{x})\mathbf{x} + \mathbf{B}(\mathbf{x})\mathbf{u} \quad (4)$$

$$\mathbf{B}(\mathbf{x}) = \begin{bmatrix} 0 & 0 & 0 & 0 \\ 0 & 0 & 0 & 0 \\ 0 & 0 & 0 & 0 \\ B_{41}(\mathbf{x}) & B_{42}(\mathbf{x}) & 0 & 0 \\ B_{51}(\mathbf{x}) & B_{52}(\mathbf{x}) & 0 & -\frac{AC_2}{m_{C2}} \\ B_{61}(\mathbf{x}) & B_{62}(\mathbf{x}) & -\frac{A_V}{m_V} & 0 \end{bmatrix}$$

$$R_{11}(\mathbf{x}) = b_{C1} + A_{C1}^2 R_{A1}(\mathbf{x}) \times \left(1 - \frac{R_{A1}(\mathbf{x})[R_{A2}(\mathbf{x}) + R_{V2} + R_V(\mathbf{x})]}{R_V(\mathbf{x})R_{\text{Total}}(\mathbf{x})} \right)$$

$$R_{22}(\mathbf{x}) = b_{C2} + A_{C2}^2 R_{A2}(\mathbf{x}) \times \left(1 - \frac{R_{A2}(\mathbf{x})[R_{A1}(\mathbf{x}) + R_{V1} + R_V(\mathbf{x})]}{R_V(\mathbf{x})R_{\text{Total}}(\mathbf{x})} \right)$$

$$R_{33}(\mathbf{x}) = b_V + \frac{A_V^2 [R_{A1}(\mathbf{x}) + R_{V1}][R_{A2}(\mathbf{x}) + R_{V2}]}{R_{\text{Total}}(\mathbf{x})}$$

$$R_{12}(\mathbf{x}) = \frac{A_{C1}A_{C2}R_{A1}(\mathbf{x})R_{A2}(\mathbf{x})}{R_{\text{Total}}(\mathbf{x})}$$

$$R_{13}(\mathbf{x}) = \frac{A_{C1}A_V R_{A1}(\mathbf{x})[R_{A2}(\mathbf{x}) + R_{V2}]}{R_{\text{Total}}(\mathbf{x})}$$

$$R_{23}(\mathbf{x}) = \frac{A_{C2}A_V R_{A2}(\mathbf{x})[R_{A1}(\mathbf{x}) + R_{V1}]}{R_{\text{Total}}(\mathbf{x})}$$

$$B_{41}(\mathbf{x}) = \frac{A_{C1}}{m_{C1}} \left(1 - \frac{R_{A1}(\mathbf{x})[R_{A2}(\mathbf{x}) + R_{V2}]}{R_V(\mathbf{x})R_{\text{Total}}(\mathbf{x})} \right)$$

$$B_{42}(\mathbf{x}) = \frac{A_{C1}R_{A1}(\mathbf{x})[R_{A2}(\mathbf{x}) + R_{V2}]}{m_{C1}R_V(\mathbf{x})R_{\text{Total}}(\mathbf{x})}$$

$$B_{51}(\mathbf{x}) = \frac{A_{C2}}{m_{C2}} \left(1 - \frac{R_{A2}(\mathbf{x})[R_{A1}(\mathbf{x}) + R_{V1}]}{R_V(\mathbf{x})R_{\text{Total}}(\mathbf{x})} \right)$$

$$B_{52}(\mathbf{x}) = \frac{A_{C2}R_{A2}(\mathbf{x})[R_{A1}(\mathbf{x}) + R_{V1}]}{m_{C2}R_V(\mathbf{x})R_{\text{Total}}(\mathbf{x})}$$

$$B_{61}(\mathbf{x}) = \frac{A_V(\mathbf{x})[R_{A1}(\mathbf{x}) + R_{A2}(\mathbf{x}) + R_{V1} + R_{V2}]}{m_V R_{\text{Total}}(\mathbf{x})}$$

$$B_{62}(\mathbf{x}) = \frac{A_V(\mathbf{x})[R_{A1}(\mathbf{x}) + R_{V1}][R_{A2}(\mathbf{x}) + R_{V2}]}{m_V R_V(\mathbf{x})R_{\text{Total}}(\mathbf{x})}$$

$$R_{\text{Total}}(\mathbf{x}) = R_{A1}(\mathbf{x}) + R_{A2}(\mathbf{x}) + R_{V1} + R_{V2} + \frac{[R_{A1}(\mathbf{x}) + R_{V1}][R_{A2}(\mathbf{x}) + R_{V2}]}{R_V(\mathbf{x})}$$

All of the model parameters are listed below and their values are estimated to order of magnitude based on physiology literature [14], [20], [21], [23]–[27] and on observable behavior.

$K_{C1} = K_{C2} \sim 10^5$ N/m	capillary wall stiffness;
$K_V \sim 10^3$ N/m	venous wall stiffness;
$m_{C1} = m_{C2} \sim 10^{-3}$ kg	capillary wall and blood inertia;
$m_V \sim 10^{-3}$ kg	venous wall and blood inertia;
$b_{C1} = b_{C2} \sim 10^4$ N · s/m	capillary wall damping;
$b_V \sim 10^2$ N · s/m	venous wall damping;
$A_{C1} = A_{C2} \sim 10^{-4}$ m ²	capillary surface area;
$A_V \sim 10^{-4}$ m ²	venous surface area;
$D_{C1} = D_{C2} \sim 10^{-5}$ m	nominal capillary diameter;
$D_V \sim 10^{-4}$ m	nominal venous diameter;
$L_{C1} = L_{C2} \sim 10^{-3}$ m	capillary length;
$L_V \sim 10^{-2}$ m	venous length;
$N_{C1} = N_{C2} \sim 10^5$	number of capillaries;
$N_V \sim 10^2$	number of small veins;
$\mu_{\text{Blood}} \sim 3 \times 10^{-3}$ Pa · s	blood viscosity;
$R_{V1} = R_{V2} \sim 10^{11}$ Pa · s/m ³	lumped venule resistance;
$P_H \sim 10^4$ Pa (gauge)	upstream blood pressure;
$P_L \sim 0$ Pa (gauge)	downstream blood pressure;

Finally, the optical portion of the model should be included as an output function relating the diameters of the capillary elements to the output of the photodetectors. For transmission of light through a solution, the Beer-Lambert Law can be applied, as shown by (5).

$$\begin{aligned} I_{\text{out}} &= I_{\text{in}} e^{-A} \\ A &= LC\varepsilon \end{aligned} \quad (5)$$

with notation defined as follows.

I_{out}	output light intensity;
I_{in}	input light intensity;
A	absorption;
L	path length;
C	concentration of absorbing substance;
$\varepsilon = \varepsilon(\lambda)$	absorption coefficient.

In the case of blood, corrections are often made for scattering effects [28]. However, in the case of capillaries, scattering is negligible, since the number of layers of blood cells is few in each capillary [21]. Furthermore, it can be assumed that the capillaries are small and evenly distributed, such that the nail bed can be treated as a continuum having a uniform blood concentration. These conditions allow us to apply the simple Beer-Lambert law to the fingernail. Since the output voltage of the photodiode circuit shown in Fig. 3 is directly proportional to the incident light intensity, (5) can be rewritten as

$$V_P = V_0 + V_1 e^{-LC\varepsilon} \quad (6)$$

where V_P is the photodetector output, V_0 is a bias voltage, and V_1 is a proportionality constant. V_0 is due to the light directly reflected back to the photodiode from the surface of the nail

without passing through the capillaries of the nail bed, and V_1 depends on the photodiode sensitivity, LED brightness, tissue absorbance, and various optical losses. The blood concentration, C can be expressed as the ratio of the blood volume in the capillaries to the tissue volume:

$$C = \frac{V_{\text{Blood}}}{V_{\text{Tissue}}} = \frac{N_C L_C \pi (D_C + x_C)^2}{4V_{\text{Tissue}}}. \quad (7)$$

Applying the above to each of the reddening and whitening zones and substituting it into (3) yields the output voltage of each photodiode:

$$\begin{aligned} V_{Pi} &= V_{0i} + V_{1i} e^{-\alpha_i (D_{Ci} + x_{Ci})^2}, \quad i = 1, 2 \\ \alpha_i &= \frac{\pi \varepsilon L_i N_{Ci} L_{Ci}}{4V_{\text{Tissue},i}}. \end{aligned} \quad (8)$$

By estimating the values of the constants in α to order of magnitude, it is possible to further simplify the optical model. Namely, the product of α and $(D_C + x_C)^2$ is on the order of 10^{-2} . Taking the first two terms of the Taylor expansion of the exponential, (8) reduces to

$$V_{Pi} = V'_{0i} - V'_{1i} (D_{Ci} + x_{Ci})^2. \quad (9)$$

Thus the output voltage of each photodetector is proportional to the square of the effective diameter of the capillary capacitance beneath it. The output function given by (9) can be applied to the states in (4) in order to simulate the photodetector response to various touch inputs. The simulations can then be compared to experimental data to empirically determine V'_0 and V'_1 for each photodetector.

B. Simulation

The hemodynamic and optical models derived above are now simulated using the parameter values given in the previous section. First, a step pressure P_{F1} is applied only at the proximal palmar surface as shown in Fig. 8. The responses of the hemodynamic and optical models for a range of equally spaced magnitudes (0.1 N/cm²) of touch pressure are shown in Fig. 10. At time $t = 0$, the positive step pressure is applied, and then at time $t = 2$ s, the pressure is stepped back to zero. As expected, the touch pressure causes the venous capacitance to contract in diameter and the capillary capacitances to expand in diameter, resulting in the reddening effect described earlier.

The results of the simulation show a characteristically nonlinear behavior. Firstly, the steady state diameters are not linearly proportional to the touch force magnitude. Secondly, the capillary diameters, which are of primary interest, respond much more sluggishly at lower force levels. In fact, the step response back to zero force is much slower than the step response up to a positive force. The venous diameter, on the other hand, responds just as quickly to the negative step as to the positive step. Therefore it is concluded that the asymmetry of the arterial behavior is related to the nonlinearity of the fluid dynamics between the arteries and veins. Specifically, the smaller fluidic resistance at low force slows the system response.

Fig. 11 shows the step response of the two photodetectors for simultaneous step inputs at both the proximal and distal palmar

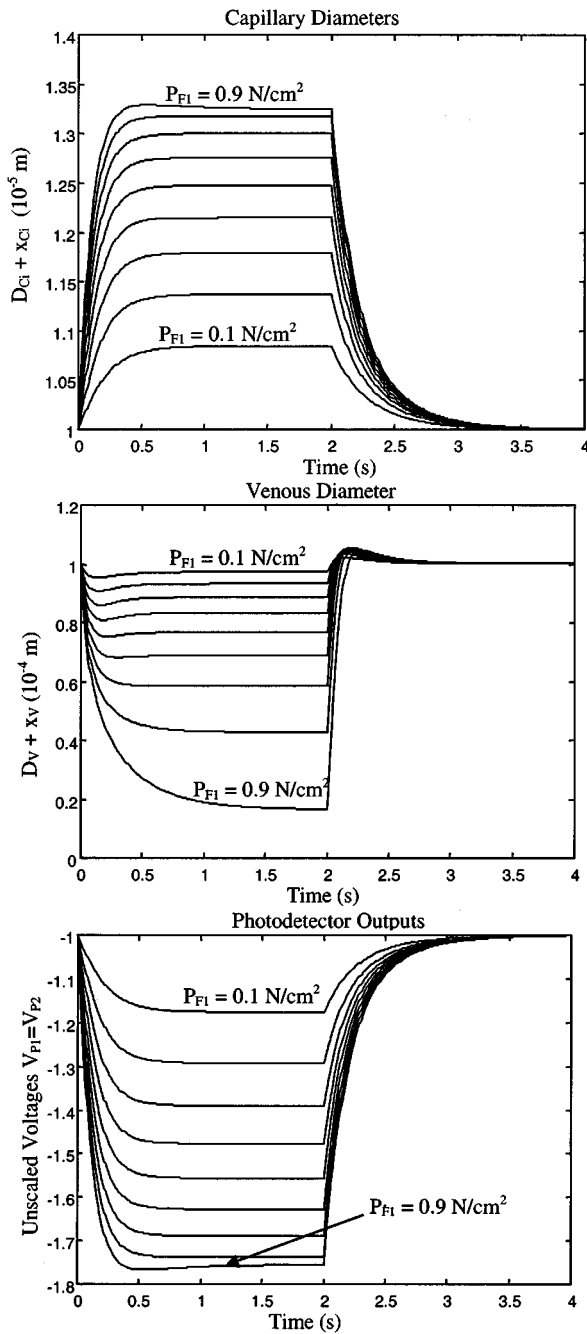


Fig. 10. Simulated dynamic step response to proximal pressure.

surfaces. At time $t = 0$, a step pressure is applied, and at time $t = 2$ s, it is released. As expected, the output of the proximal photodetector decreases (reddening effect) and the output of the distal photodetector increases (whitening effect). While the output of the proximal photodetector still behaves nonlinearly, the output of the distal photodetector demonstrates a more linear behavior, with approximately equal loading and unloading response times. This indicates that the response of the distal capillary capacitance is dominated by the direct mechanical influence from the touch pressure, rather than by the fluidic interactions.

Fig. 12 shows the steady-state relationships between the photodetector outputs and the touch pressure inputs. When touch

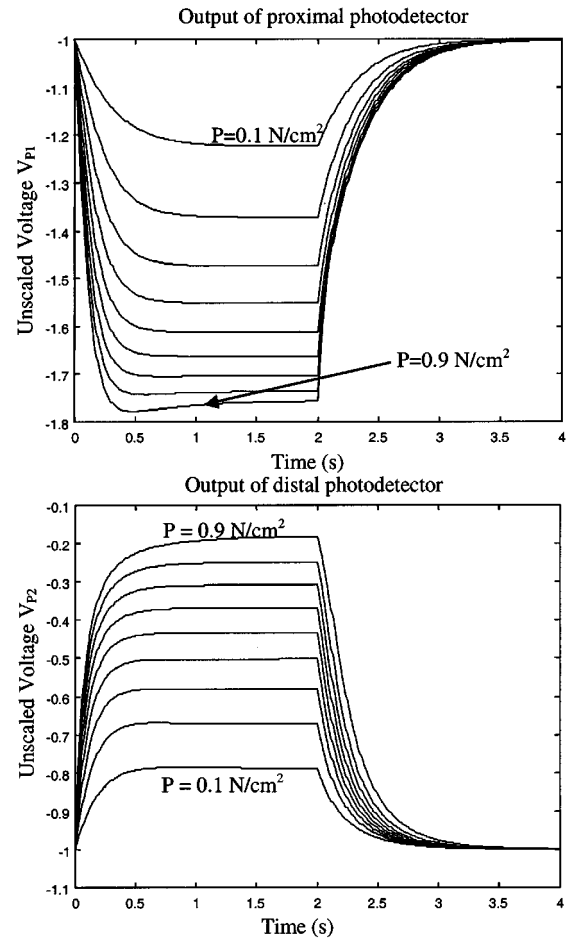


Fig. 11. Simulated dynamic step response to proximal and distal pressure.

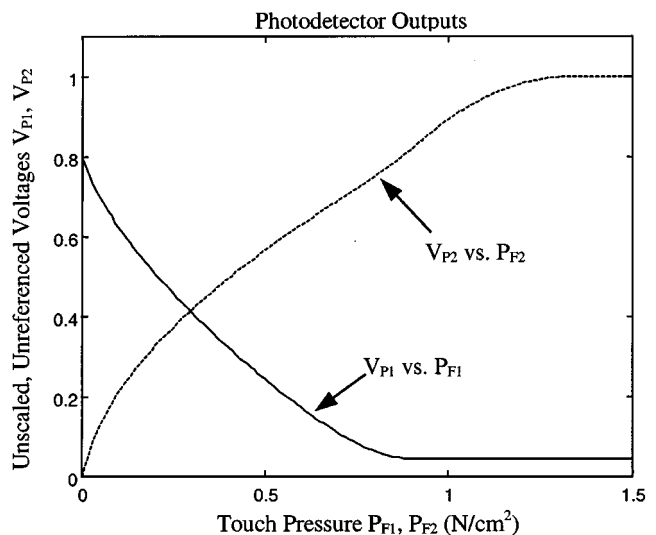


Fig. 12. Simulated steady-state relationships.

pressure P_{F1} is applied at the proximal surface, the proximal photodetector voltage V_{P1} decreases roughly linearly and then levels off at approximately 1 N/cm^2 of touch pressure. When touch pressure P_{F2} is applied at the distal surface, the distal photodetector voltage V_{P2} at first increases steeply up to 0.1

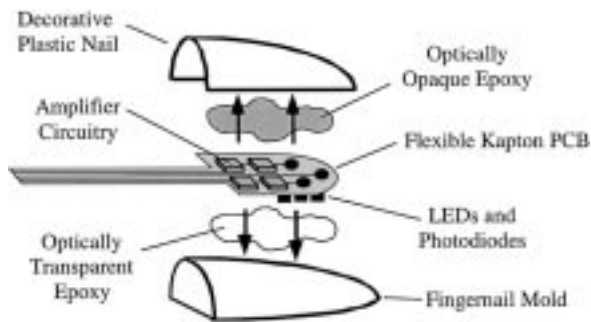


Fig. 13. Prototype design for the fingernail touch sensor.

N/cm^2 , then gradually increases linearly, and finally levels off just beyond 1 N/cm^2 .

V. PROTOTYPING AND EXPERIMENT

A. Prototyping

In designing a prototype of the fingernail sensor, there are a number of critical issues to be addressed.

1) *Size and Profile:* The sensors should be thin and unobtrusive. Using miniaturized optical components and circuitry, they could be disguised as a decorative fingernail such as those commonly worn on the natural fingernail.

2) *Means of Attachment:* To minimize sensor noise from motion artifact, the sensors should be attached rigidly to the fingernail. However, the interface must be optically transparent to maximize the sensitivity of the sensor.

3) *Shielding of Ambient Light:* To reduce sensor noise from ambient lighting, the photodiodes should be optically shielded from above. They should also be shielded from the side to prevent direct illumination from the LEDs, which would result in a large unwanted DC voltage.

4) *Signal Processing and Transmission:* The op amp stage shown in Fig. 3 should be located close to the photodiodes so that the sensor signals are amplified before being transmitted over a long distance. However, to minimize the size and complexity of the sensor, all other signal processing can be done after transmitting the signals away from the fingernail.

Fig. 13 shows a conceptual design that aims to meet the aforementioned requirements. In order to minimize size and profile, miniaturized optical and electrical components are mounted using wire bonding to a thin flexible Kapton printed circuit board. The optical components are placed on the bottom and covered with a protective layer of optically transparent epoxy, which is molded to the shape of the wearer's fingernail. A barrier of optically opaque epoxy is placed between the photodetectors and LEDs. The amplifier components are placed on top, and then the entire top surface is coated with optically opaque epoxy for shielding of ambient light, and finally a decorative plastic nail is placed on top for aesthetic purposes. After amplification, the signals travel through the thin Kapton strip to the wearer's wrist. The sensor can be attached to the wearer's fingernail using a double-sided transparent adhesive.

Prototype fingernail sensors have been fabricated and assembled, as shown in Fig. 14. For the prototype shown here, two photodiode arrays of dimension $4 \text{ mm} \times 1 \text{ mm}$ are attached end

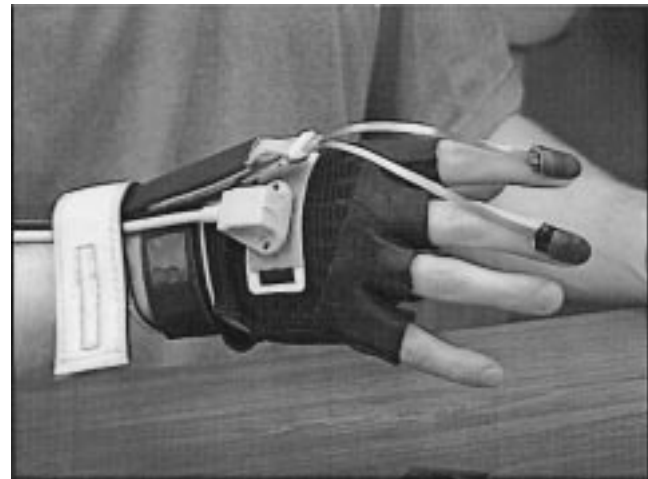


Fig. 14. Implementation of fingernail touch sensors.

to end on the bottom side. Up to 8 of the 32 total photodiodes can be wired up at once, resulting in up to eight sensing locations along the length of the fingernail. Up to three LEDs of dimension $0.25 \text{ mm} \times 0.25 \text{ mm}$ can be placed in flexible locations beside the photodiode arrays.

B. Experiment

In order to test the validity of the model, static and dynamic experiments are performed using the prototype nail sensors. Data is collected for eight human subjects of varying gender and skin color. Ideally, a subject's finger could be immobilized while known forces are mechanically applied; however it is extremely difficult to immobilize the finger without affecting the blood flow. Therefore for these experiments, the subjects are instructed to apply the forces themselves against a flat padded surface. A strain-gauge force sensor placed underneath the surface directly measures the applied touch force. The strain-gauge readings are fed back to the subject using a visual display, allowing the subjects to monitor and control the applied force.

Fig. 15 shows the experimental steady-state response of a proximal photodetector to touch force applied normally at the proximal palmar surface of the fingertip. For this experiment, the subject is instructed to slowly cycle the force between 0 and 2 N at approximately 0.05 Hz. The plot shows the average results of three cycles for each subject, and the average of all the subjects. As expected, an approximately linear decrease is observed up to about 1 N, past which the output exhibits a non-linear leveling off. By tuning the previously unknown offset and scaling parameters in (9), the simulated response can be fitted to the experimental average, and is plotted overtop as a dashed line for comparison. The magnitude and range of sensitivity vary across the subjects, but the behavior is similar. Certain subjects show a slight increase in voltage at large force due to encroachment of the whitening zone, an effect not included in the model.

Fig. 16 shows the corresponding dynamic response to proximal touch force for subject 2 (dark skin, static sensitivities close to average) and subject 3 (light skin, static sensitivities far from average). The subjects are instructed to apply a step force as quickly as possible, maintain it, and then release as quickly

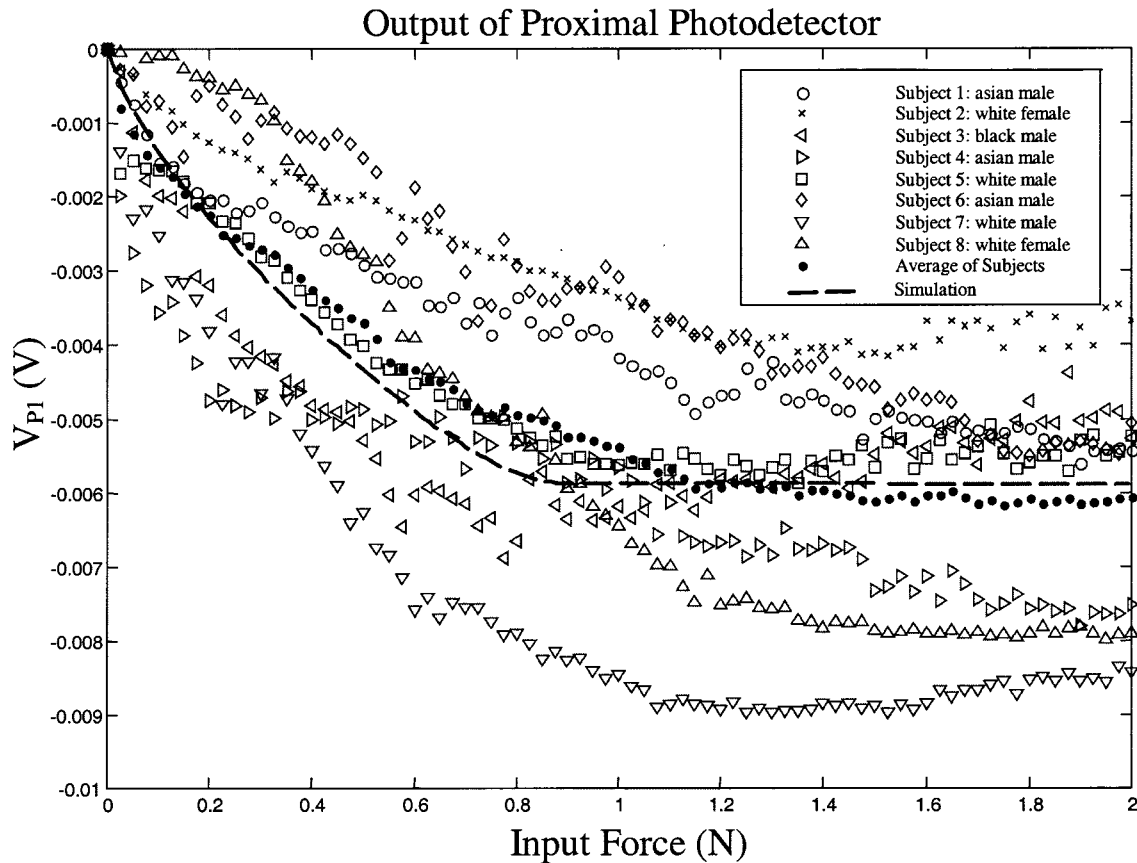


Fig. 15. Experimental static relationship for proximal pressure.

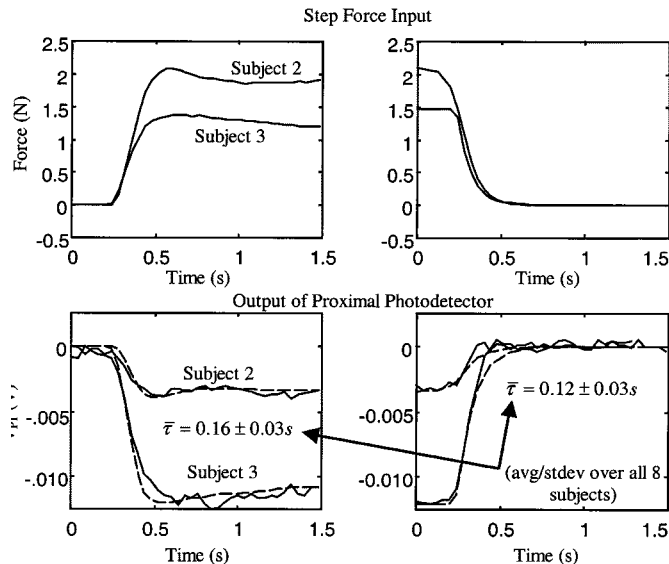


Fig. 16. Experimental dynamic response to proximal pressure.

as possible. Although the sensitivities differ, all eight subjects show time constants that are at least as fast as that of the measured input force (average $\tau = 0.16$ s for loading/ 0.12 s for unloading). The model time constants are first tuned to match the subjects by adjusting the stiffness and damping parameters of (3) within an order of magnitude. The model is then calibrated to each subject by tuning the scaling and offset parameters of

(9). The model response to the measured forces is simulated and plotted overtop as dashed lines for subjects 2 and 3.

Fig. 17 shows the experimental steady-state response of a distal photodetector to touch force applied at the distal palmar surface of the fingertip. As expected, an approximately linear behavior is observed up to about 1 N, past which the output exhibits a nonlinear leveling off. In this case, while the magnitude of sensitivity varies across subjects, the range of sensitivity is very consistent. The slightly positive slope beyond 1 N is a result of the widening of the whitening band, an unmodeled effect.

Fig. 18 shows the corresponding dynamic response to distal touch force for the same two subjects. As before, the model response is calibrated to the experimental response for each subject and plotted overtop as dashed lines. Compared to proximal touching, the time constants here are noticeably longer (average $\tau = 0.18$ s for loading/ 0.36 s for unloading). On average, subjects exhibit a much longer time constant for unloading than loading, most likely due to unmodeled creep behavior of the distal finger pulp.

At this point, the principal limitation in comparing simulations and experiments is that the simulations assume that two distinct, uniformly distributed pressures are applied to the proximal and distal palmar surfaces of the fingertip; whereas in our experiments, a single lumped force is applied and it is not known how the pressure is distributed across the fingertip. However, the comparison does show agreement between experiment and simulation in terms of general static and dynamic behavior.

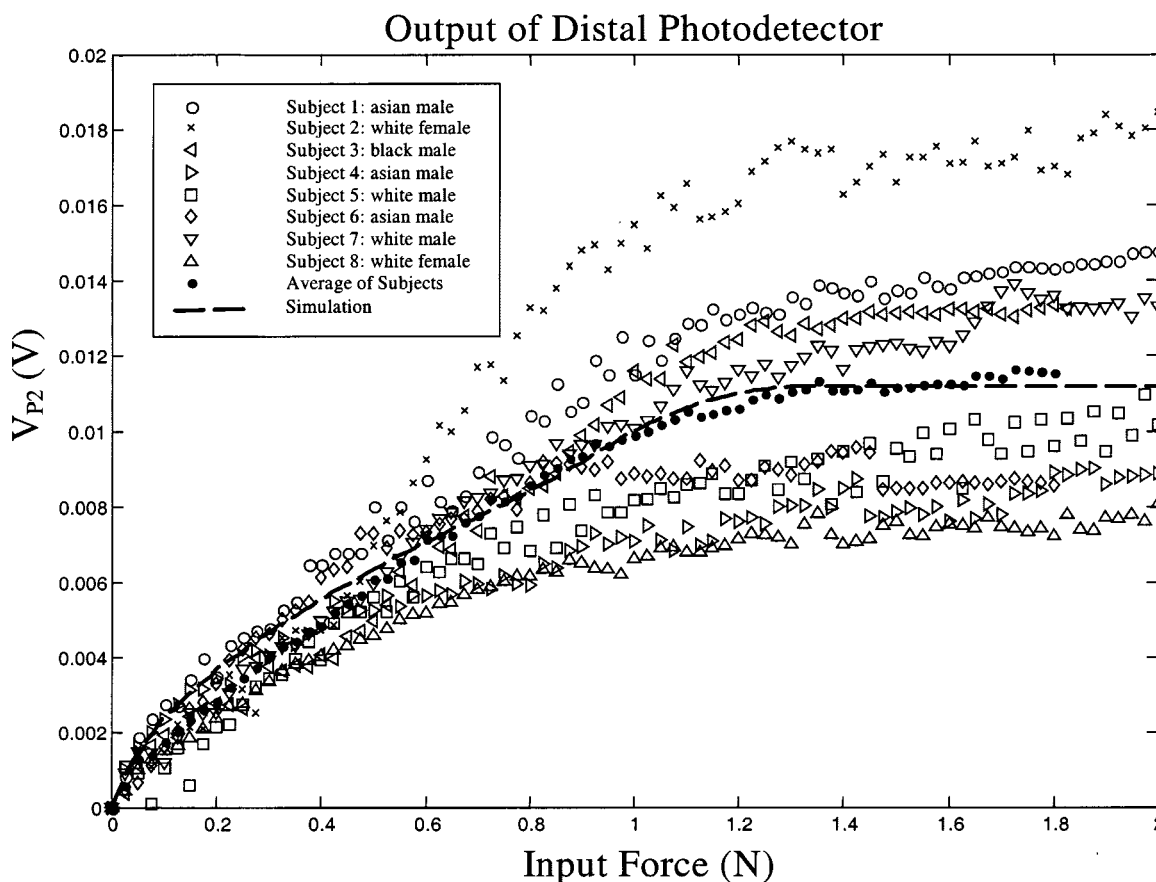


Fig. 17. Experimental static relationship for distal pressure.

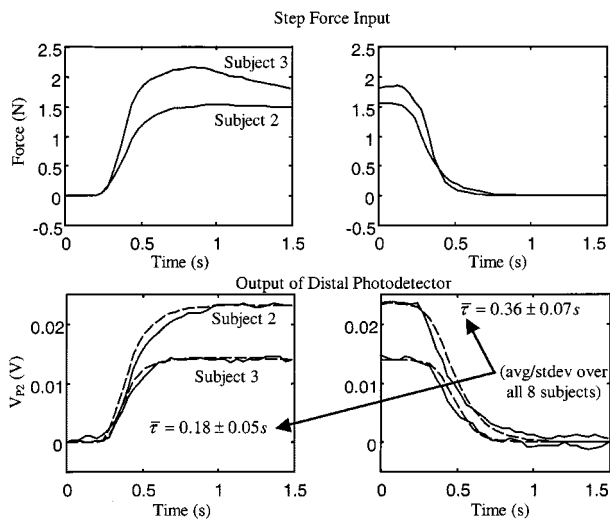


Fig. 18. Experimental dynamic response to distal pressure.

VI. CONCLUSION

A new type of touch sensor for detecting contact pressure at human fingertips has been presented. Fingernails are instrumented with arrays of micro LEDs and photodetectors in order to measure changes in reflection intensity when the fingers are pressed against a surface. Observable changes in fingernail coloration were described and used to create an anatomically

and physiologically based, lumped-parameter, hemodynamic model, in order to understand the relationship between touch force input and reflection intensity output. The model was simulated and compared to experimental data for two sensing locations along the length of the fingernail, using both static and dynamic experiments. All eight subjects show the same key static and dynamic traits. Static experiments all show fairly linear sensitivities to touch forces in the range of 0–1 N. Dynamic experiments show that the time constants of the system are generally between 0.1–0.4 s, which proves the feasibility of the sensor for measuring rapid touching action. By tuning a few parameters to match the time constants and scaling, the model can be successfully calibrated to each user, and ultimately used to predict touch force based on sensor output. At this stage, the model is sufficient to explain the observed behavior but is limited to only two discrete outputs and inputs. With a more sound treatment of tissue mechanics, the complexity of the model can be expanded to deal with a greater array of photodetectors as well as a more continuous distribution of contact forces, perhaps including even shear forces.

Unlike traditional electronic gloves, in which sensor pads are placed between the fingers and the environment surface, this new sensor allows the fingers to directly contact the environment without obstructing the human’s natural haptic senses. This new technology could be used for robot skill acquisition, teleoperation, human behavior monitoring, or even recording of chiropractic or surgical skills, where neither the patient nor

the physician's fingers can be covered with sensors. By instrumenting the human in an unobtrusive manner, a new approach to human—machine interface can be explored. "Virtual switches," for example, replace traditional switches with mere images of switches on a surface, activated by signals from the nail sensors and a position tracker [29]. This, in turn, would open up new possibilities in human—robot interactions.

REFERENCES

- [1] B. McCarragher, "Force sensing from human demonstration using a hybrid dynamical model and qualitative reasoning," *Proc. IEEE Int. Conf. Robot. Automat.*, vol. 1, pp. 557–563, 1994.
- [2] S. Sato, M. Shimojo, Y. Seki, A. Takahashi, and S. Shimuzu, "Measuring system for grasping," *Proc. IEEE Int. Workshop Robot Human Commun.*, pp. 292–297, 1996.
- [3] I. Kim and H. Inooka, "Determination of grasp forces for robot hands based on human capabilities," *Contr. Eng. Practice*, vol. 2, no. 3, pp. 415–420, 1994.
- [4] M. Castro and A. Cliquet Jr., "A low-cost instrumented glove for monitoring forces during object manipulation," *IEEE Trans. Rehab. Eng.*, vol. 5, pp. 140–147, 1997.
- [5] H. Yun, D. Cannon, A. Freivalds, and G. Thomas, "An instrumented glove for grasp specification in virtual-reality-based point-and-direct telerobotics," *IEEE Trans. Syst. Man, Cybern. B*, vol. 27, pp. 835–846, 1997.
- [6] S. Mascaro and H. Asada, "Hand-in-glove human-machine interface and interactive control: Task process modeling using Petri Nets," *Proc. IEEE Int. Conf. Robot. Automat.*, vol. 2, pp. 1289–1295, 1998.
- [7] J. G. Webster, Ed., *Tactile Sensors for Robotics and Medicine*. New York: Wiley, 1988.
- [8] D. J. Sturman and D. Zeltzer, "A survey of glove-based input," *IEEE Comp. Graph. Appl.*, vol. 14, pp. 30–39, 1994.
- [9] D. Beebe, D. Denton, R. Radwin, and J. Webster, "A silicon-based tactile sensor for finger-mounted applications," *IEEE Trans. Biomed. Eng.*, vol. 45, pp. 151–159, 1998.
- [10] T. R. Jensen, R. G. Radwin, and J. G. Webster, "A conductive polymer sensor for measuring external finger forces," *J. Biomech.*, vol. 24, no. 9, pp. 851–858, 1991.
- [11] R. Liu, L. Wang, and D. Beebe, "Progress toward a smart skin: Fabrication and preliminary testing," *Proc. 20th Annual Int. Conf. IEEE Eng. Med. Biol. Soc.*, vol. 20, no. 4, pp. 1841–1844, 1998.
- [12] A. P. Spence, *Basic Human Anatomy*. Menlo Park, CA: Benjamin/Cummings, 1982.
- [13] K. K. Tremper and S. J. Barker, "Pulse oximetry," *Anesthesiology*, vol. 70, no. 1, pp. 98–108, 1989.
- [14] R. Baran *et al.*, *Diseases of the Nails and Their Management*, 2nd ed, R. Baran and R. P. R. Dawber, Eds, Oxford: Blackwell Scientific, 1994.
- [15] R. V. Krstic, *Human Microscopic Anatomy: An Atlas for Students of Medicine and Biology*. New York: Springer-Verlag, 1991.
- [16] R. Wolfram-Gabel and H. Sick, "Vascular networks of the periphery of the fingernail," *J. Hand Surgery*, vol. 20B, no. 4, pp. 488–492, 1995.
- [17] M. H. Flint, "Some observations on the vascular supply of the nail bed and terminal segments of the finger," *British J. Hand Surgery*, vol. 8, pp. 186–195, 1956.
- [18] E. G. Zook, A. L. Van Beek, R. C. Russell, and M. E. Beatty, "Anatomy and physiology of the perionychium: A review of the literature and anatomic study," *J. Hand Surgery*, vol. 5, no. 6, pp. 528–536, 1980.

- [19] D. O. Smith, O. Chikayoshi, C. Kimura, and K. Toshimori, "Artery anatomy and tortuosity in the distal finger," *J. Hand Surgery*, vol. 16A, pp. 297–302, 1991.
- [20] —, "The distal venous anatomy of the finger," *J. Hand Surgery*, vol. 16A, pp. 303–307, 1991.
- [21] A. C. Guyton, *Textbook of Medical Physiology*. Philadelphia, PA: Saunders, 1981.
- [22] M. A. Srinivasan, "Surface deflection of primate fingertip under line load," *J. Biomech.*, vol. 22, no. 4, pp. 343–349, 1989.
- [23] A. Bollinger, P. Butti, J.-P. Barras, H. Trachsler, and W. Siegenthaler, "Red blood cell velocity in nailfold capillaries of man measured by a television microscopy technique," *Microvasc. Res.*, vol. 7, pp. 61–72, 1974.
- [24] J. D. Coffman and A. S. Cohen, "Total and capillary fingertip blood flow in Raynaud's phenomenon," *N. Engl. J. Med.*, vol. 285, no. 5, pp. 259–263, 1971.
- [25] F. Brunelli and G. Brunelli, "Vascular anatomy of the distal phalanx," in *Fingertip and Nailbed Injuries*, G. Foucher, Ed, Edinburgh, U.K.: Churchill Livingstone, 1991, pp. 1–9.
- [26] H. R. Maricq, "Capillary pattern in familial schizophrenics: A study of nailfold capillaries," *Circulation*, vol. 27, pp. 406–413, 1963.
- [27] D. Richardson, "Relationship between digital artery and nailfold capillary flow velocities in human skin," *Microcirculation*, vol. 2, no. 3, pp. 283–296, 1982.
- [28] J. M. Steinke and A. P. Shepherd, "Role of light scattering in whole blood oximetry," *IEEE Trans. Biomed. Eng.*, vol. 33, pp. 294–301, 1986.
- [29] S. Mascaro and H. Asada, "Virtual switch human-machine interface using fingernail touch sensors," *Proc. IEEE Int. Conf. Robot. Automat.*, vol. 4, pp. 2533–2538, 1999.

Stephen A. Mascaro (S'96) was born in Nyack, NY, in 1972. He received the B.A. degree in physics from Houghton College, Houghton, NY, the B.S. degree in mechanical engineering from Clarkson University, Potsdam, NY, and the M.S. degree in mechanical engineering from the Massachusetts Institute of Technology (MIT), Cambridge, in 1995, 1995, and 1997, respectively. He is currently working toward the Ph.D. degree in mechanical engineering at the d'Arbelloff Laboratory for Information Systems and Technology of MIT. His research interests include system dynamics and control, robotics, human-machine interaction, haptics, biomechanical and physiological modeling, and wearable sensors.

H. Harry Asada (A'85) received the B.S., M.S., and Ph.D. degrees all in mechanical engineering, from Kyoto University, Kyoto, Japan, in 1973, 1975, and 1979, respectively.

From 1978 to 1982, he was a Research Associate with Kyoto University. From 1982 to 1985, he was an Assistant Professor with the Department of Mechanical Engineering, Massachusetts Institute of Technology (MIT), Cambridge. From 1985 to 1988, he was an Associate Professor with the Department of Applied Systems Science, Kyoto University. In January 1989, he joined MIT, where he is currently the Ford Professor of Mechanical Engineering and Director of the d'Arbelloff Laboratory for Information Systems and Technology. His general areas of interest are robotics, systems and control, mechanical design, biomedical engineering, and information technology.